THE ASTROPHYSICAL JOURNAL, 556:958–969, 2001 August 1

HIGH-RESOLUTION NEAR-INFRARED IMAGES AND MODELS OF THE CIRCUMSTELLAR DISK IN HH 30

ANGELA S. COTERA,[1] BARBARA A. WHITNEY,[2] ERICK YOUNG,[1] MICHAEL J. WOLFF,[2] KENNETH WOOD,[3] MATTHEW POVICH,[3] GLENN SCHNEIDER,[1,4] MARCIA RIEKE,[1,4] AND RODGER THOMPSON[1,4]

Received 2000 November 21; accepted 2001 April 9

ABSTRACT

We present *Hubble Space Telescope* near-infrared camera and multiobject spectrometer observations of the reflection nebulosity associated with the T Tauri star HH 30. The images show the scattered-light pattern characteristic of a highly inclined, optically thick disk with a prominent dust lane whose width decreases with increasing wavelength. The reflected nebulosity exhibits a lateral asymmetry in the upper lobe on the opposite side to that reported in previously published Wide Field Planetary Camera 2 images. The radiation transfer model that most closely reproduces the data has a flared accretion disk with dust grains larger than standard interstellar medium grains by a factor of approximately 2.1. A single hot spot on the stellar surface provides the necessary asymmetry to fit the images and is consistent with previous modeling of the light curve and images. Photometric analysis results in an estimated extinction of $A_V \gtrsim 80$; however, since the photometry measures only scattered light rather than direct stellar flux, this a lower limit. The radiative transfer models require an extinction of $A_V = 7900$.

Subject headings: accretion, accretion disks — radiative transfer — stars: individual (HH 30) — stars: pre–main-sequence — stars: rotation — stars: spots

On-line material: color figures

1. INTRODUCTION

Theory has long predicted that dense equatorial circumstellar accretion disks are formed during the collapse of low-mass stars (Cameron 1962, 1973; Wetherill 1980; Cassen & Moosman 1981; Terebey, Shu, & Cassen 1984; Adams & Shu 1986, and references therein). The observational evidence for such disks has been inferred from the signature of excess infrared radiation arising from starlight reprocessed by dust and the liberation of accretion luminosity (Lynden-Bell & Pringle 1974; Lada & Wilking 1984; Lada 1987; Kenyon & Hartmann 1987) and the spectroscopic signatures of accretion (Hartmann & Kenyon 1985; Bertout 1989 and references therein). Radio and millimeter observations have successfully imaged the disks, allowing an investigation of their velocity and density structures (Beckwith et al. 1990; Beckwith & Sargent 1993; Koerner, Sargent, & Beckwith 1993; Koerner & Sargent 1995). Radiation transfer models predicted that the scattered light from disks could be imaged in systems in which the disk is viewed close to edge-on to our line of sight, blocking light from the central star (Whitney & Hartmann 1992). Recent high-resolution *Hubble Space Telescope* (*HST*) Wide Field Planetary Camera 2 (WFPC2) images have discovered just such signatures of highly inclined disks around T Tauri stars (Burrows et al. 1996; Stapelfeldt et al. 1998; Krist et al. 2000).

The first, and perhaps the most stunning, example of a disk to be detected in this manner was that of HH 30 by Burrows et al. (1996). Their WFPC2 images resolved the HH 30 nebulosity into the characteristic nebular pattern of an edge-on disk: two reflection nebulae separated by a dark dust lane (Whitney & Hartmann 1992). Their images also show the strong jet present in HH 30, which is found to be highly collimated deep within the disk. Burrows et al. constructed scattered-light models of a flaring disk for their HH 30 observations, estimating a disk mass of around $10^{-3}\ M_\odot$ and a scale height of 15 AU at a radius of 100 AU. Their modeling of the scattered-light images required the dust grains to have a scattering phase function that is more forward-throwing than typical interstellar medium (ISM) grains. Wood et al. (1998) investigated whether protostellar envelopes could produce the scattered-light pattern associated with HH 30 and concluded that only a very tenuous circumstellar envelope is required in addition to the disk. Wood et al. (1998) estimated a disk mass of $2.5 \times 10^{-4}\ M_\odot$. The mass estimates of both Wood et al. and Burrows et al. are only sensitive to small grains within the disk and are dependent on the assumed gas-to-dust mass ratio and dust composition. Since the optical opacities of large grains, rocks, and planetesimals are small, they have no effect on the optical and near-infrared (NIR) scattered light and are not well accounted for in these mass estimates. If the wavelength dependence typical for ISM grains is assumed for the dust opacity, Wood et al. (1998) also predicted that HH 30 should appear almost pointlike in the K band (2.2 μm)—a feature that we shall address in some detail in this paper.

The *HST* WFPC2 observations of HH 30 also showed that the scattered-light pattern is highly variable, having changed considerably in brightness between the two observations presented by Burrows et al. (1996). The variability of the scattered-light nebula in HH 30 is not surprising given that photometric variability is a ubiquitous characteristic of T Tauri stars, with *periodic* photometric variability having now been detected in hundreds of systems (see, e.g., Bouvier et al. 1993; Choi & Herbst 1996; Wichmann et al. 1998). In classical T Tauri stars, such variability is attributed to hot and cool spots on the stellar surface (see, e.g.,

[1] Steward Observatory, University of Arizona, 933 North Cherry Avenue, Tucson, AZ 85721; cotera@as.arizona.edu, eyoung@as.arizona.edu, gschneider@stsci.edu, mrieke@as.arizona.edu, rthompson@as.arizona.edu.

[2] Space Science Institute, 3100 Marine Street, Suite A353, Boulder, CO 80303; bwhitney@colorado.edu, wolff@colorado.edu.

[3] Harvard-Smithsonian Center for Astrophysics, 60 Garden Street, Cambridge, MA 02138; kwood@cfa.harvard.edu.

[4] Department of Astronomy, 933 North Cherry Avenue, University of Arizona, Tucson, AZ 85721.

Bouvier et al. 1993; Kenyon et al. 1994; Herbst et al. 1994; Eaton, Herbst, & Hillenbrand 1995; Choi & Herbst 1996), with magnetic accretion models naturally providing these hot spots (Ghosh & Lamb 1979a, 1997b; Königl 1991; Shu et al. 1994; Ostriker & Shu 1995; Najita 1995). Wood & Whitney (1998) investigated the observational signatures of stellar hot spots, finding that the variations in the HH 30 observations by Burrows et al. (1996) could be explained with such a model. They also predicted that the disk should brighten asymmetrically during the stellar rotation period. Such a lateral asymmetry was found by Stapelfeldt et al. (1999) in another WFPC2 pointing at HH 30. Wood & Whitney modeled the asymmetry with a hot spot model and found that the asymmetric brightening is best reproduced with a single large hot spot. More recently, Wood et al. (2000) presented ground-based *VRI* monitoring of HH 30 showing that it is highly variable by up to 1.5 mag over timescales of a few days, and they modeled the variability as arising from a single hot spot.

In order to extend these fruitful investigations of a star-plus-disk system to longer wavelengths, we have obtained *HST* near-infrared camera and multiobject spectrometer (NICMOS) images of HH 30. We present the highest resolution NIR images of this object to date and the first NIR images to resolve the dust lane. In § 2 the observations and the data reduction techniques are discussed, and the resulting images are presented. In § 3 the observed morphology, photometry, and the extinction based on the observations are considered. In § 4 models assuming that a single hot spot provides the illumination asymmetry are fitted to the data, a dust opacity law that is flatter than interstellar (implying larger grains) is shown to be appropriate, and an extinction through the disk of about $A_V = 7900$ is derived. In § 5 we present our main conclusion—multiwavelength imagery provides a powerful tool for probing the dust opacity in protostellar disks.

2. OBSERVATIONS AND DATA REDUCTION

The observations were made using NICMOS camera 2, which has a nominal plate scale of $0\farcs0755 \pm 0\farcs005$ pixel^{-1} to obtain diffraction limited images with a measured FWHM of $0\farcs11$ at 1.104 μm. At the distance of HH 30 (140 pc; Elias 1978), this corresponds to an angular resolution of $\sim$15 AU. The observations were made on 1997 September 29. Five filters were selected for observation: F110W, F160W, F187N, F204M, and F212N. Information on the effective wavelengths for these nonstandard filters, the FWHM of the filter functions, and other relevant parameters are presented in Table 1. Images were taken with all five filters sequentially at each of four dither positions. Total integration times for each filter are given in Table 1. Frames used for dark subtraction were taken at the end of the observations.

The data were reduced using the IRAF data reduction package NICRED written for *HST* NICMOS data (McLeod 1997). Darks for F110W, F160W, and F187N were created using the observed dark frames with the routine NICSKYDARK, which is part of the NICRED package. Dark frames for F204M and F212N were created using a few of the dark frames and the actual data frames using NICSKYDARK. The flats used were those produced by M. Rieke (1999, private communication) for use with the NICMOS data. After dark subtraction and flat-fielding, the images were cleaned for any additional bad pixels by hand using the IRAF routine IMEDIT.

The NICMOS pixels are nonsquare by $\sim$1%, and prior to shifting and adding, the pixels were rectified using interactive data language (IDL) procedures developed for the Image Display Paradigm 3 (IDP3) software package at Steward Observatory specifically for use with the NICMOS data (Stobie et al. 1999). IDP3 allows for interactive registration and quantitative analysis, such as polygon photometry, of images using IDL widgets.[5] After rectification, additional routines developed at Steward Observatory, NICMOSAIC and NICSTIKUM, were use to shift and add the images, respectively. NICMOSAIC performs the shifts by aligning them using the world coordinate system (WCS) values and then allows for interactive adjustments to better align the images if necessary. *HST* pointing was found to be sufficient for these observations, and no alignment other than the WCS was used. The routine NICSTIKUM was used to co-add the data using the shifts determined by NICMOSAIC. NICSTIKUM produced images with higher signal-to-noise ratios than the IRAF routine IMCOMBINE and were much smoother along the edges . The combined images were then flux-calibrated using the latest available values derived by M. Rieke for use with NICMOS data (M. Rieke 1999, private communication; see Table 1). A three-color composite image using the data from the wide and medium filters is presented in Figure 1. In order to compare these observations with previous WFPC2 results, we also present a three-color composite image that combines the WFPC2 F675W image taken in 1998 December (K. R. Stapelfeldt 2000, private communication) with the NICMOS F110W and F204M images taken in 1997 September (Fig. 2). Given the time variability of the object (Stapelfeldt et al. 1999), the opposing asymmetries are not unexpected.

Since no narrowband continuum filters adjacent to the F212N and F187N filter observations were taken because of time constraints, a method had to be developed to provide a best empirical estimate of the continuum in the narrowband filters using the F204M and F160W filters for

[5] IDP3 is publicly available at http://nicmos.as.arizona.edu/software/idl-tools/toollist.cgi.

TABLE 1

SUMMARY OF NICMOS OBSERVATIONS

Filter	$\lambda_{\rm eff}$ (μm)	$\Delta\lambda$ (μm)	Zero-Magnitude Flux (Jy)	Jy (ADU s^{-1})$^{-1}$ ($\times 10^{-6}$)	Integration Time (s)	A_λ/A_V
F110W.....	1.104	0.592	1775	2.031	64	0.334
F160W.....	1.593	0.403	1083	2.190	64	0.187
F187N	1.874	0.019	825	41.07	144	0.140
F204M.....	2.033	0.105	735	7.711	112	0.124
F212N	2.121	0.021	698	39.17	160	0.117

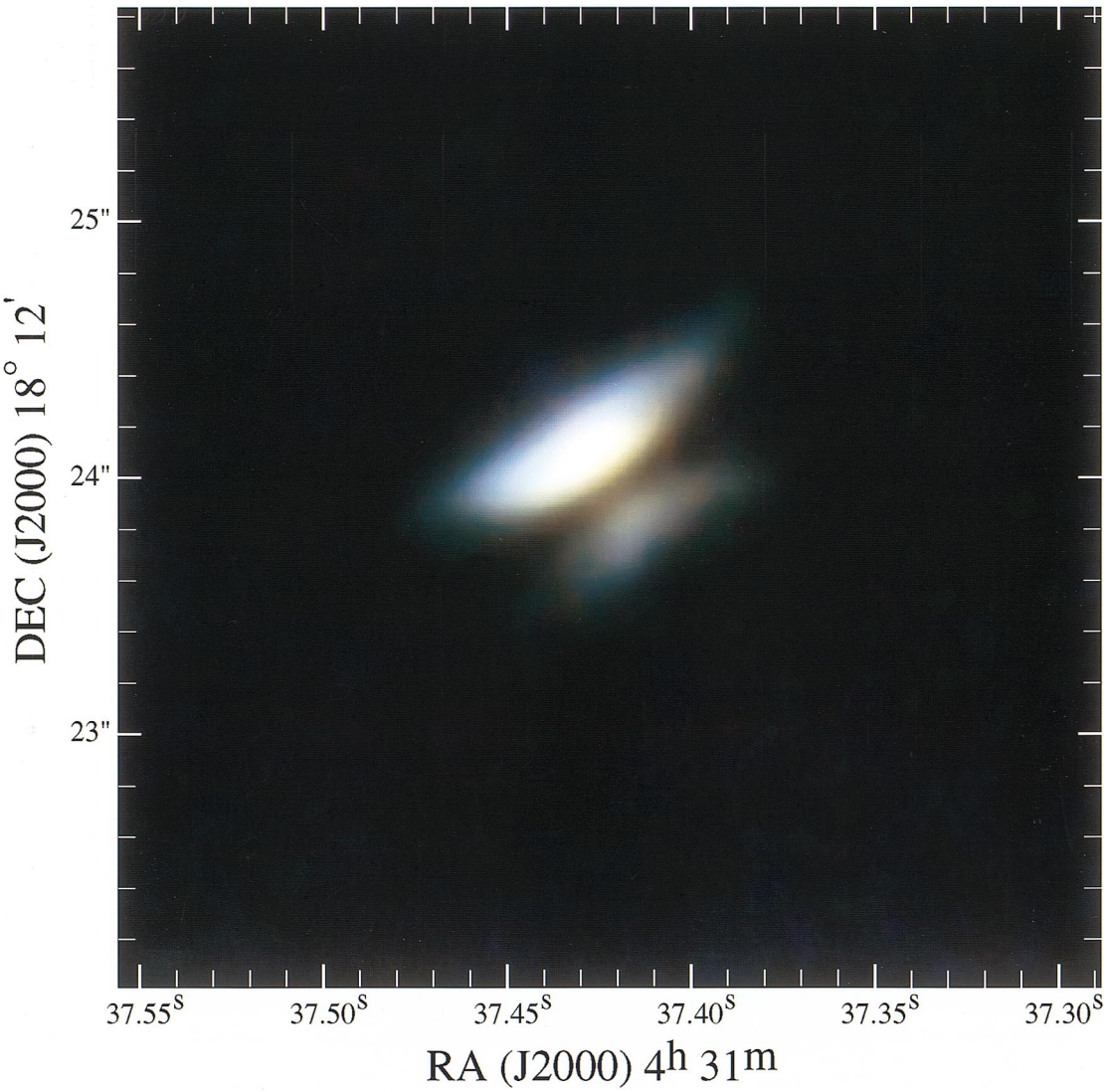

FIG. 1.—Three-color composite image of HH 30. F110W is blue, F160W is green, and F204M is red. A schematic of the disk and reflection nebulae is presented in Fig. 5.

the continuum. At first, only the F204M filter was used, but since HH 30 varies considerably with wavelength, the results for the F187N filter were unsatisfactory. A combination of the F160W and F204M images was also tried, but since we do not know the intrinsic colors of HH 30, we could not derive a credible method for weighting the filters. In the end, a semiempirical method was chosen. The filter closest in wavelength to the narrowband observation was selected as the continuum image. This "continuum" image was then subtracted from the narrowband image interactively using IDP3. Using both the region around HH 30 and a serendipitous star within the frame for statistical calculations, the continuum image was incrementally scaled until the statistical variance in the subtracted image was minimized. After subtraction, the standard deviation off source, σ, was 4.7×10^{-4} mJy pixel^{-1} at 1.87 μm and 3.3×10^{-4} mJy pixel^{-1} at 2.12 μm. The peak flux on source was 4.7×10^{-3} mJy at 1.87 μm and 5.5×10^{-3} mJy pixel^{-1} at 2.12 μm. The resulting images are presented in Figures 3 and 4.

3. OBSERVATIONAL RESULTS

Figure 1 shows that although HH 30 appears roughly symmetric, there are, in fact, asymmetries around both the axis of the dust midplane (because of the inclination of the disk) and the jet axis (similar to the lateral asymmetry reported by Stapelfeldt et al. 1999). These observed asymmetries are wavelength-dependent—the predicted decrease in the width of the dust lane with increasing wavelength is seen, but there is also a shift in the peak of the scattered light with wavelength. To both quantify this asymmetry and to insure that accurate three-color photometry could be performed, the FWHMs of the F110W and F160W images were convolved to match the FWHM of the F204M image using the IRAF package GAUSS. The serendipitous stellar point source in the frames was used to insure that the convolved point-spread functions (PSFs) were correctly matched across the filters. In addition, to facilitate accurate measurements of the physical dimensions of both the disk and reflection nebula, the images were resampled in IDP3 by a factor of 4 using bicubic interpolation.

In an effort to provide a concise discussion of the morphology and observational results, a schematic of the nebula is presented in Figure 5. The dust lane, two lobes of the reflection nebula and jet, suggests an internally consistent coordinate system, with the minimum of the dust lane

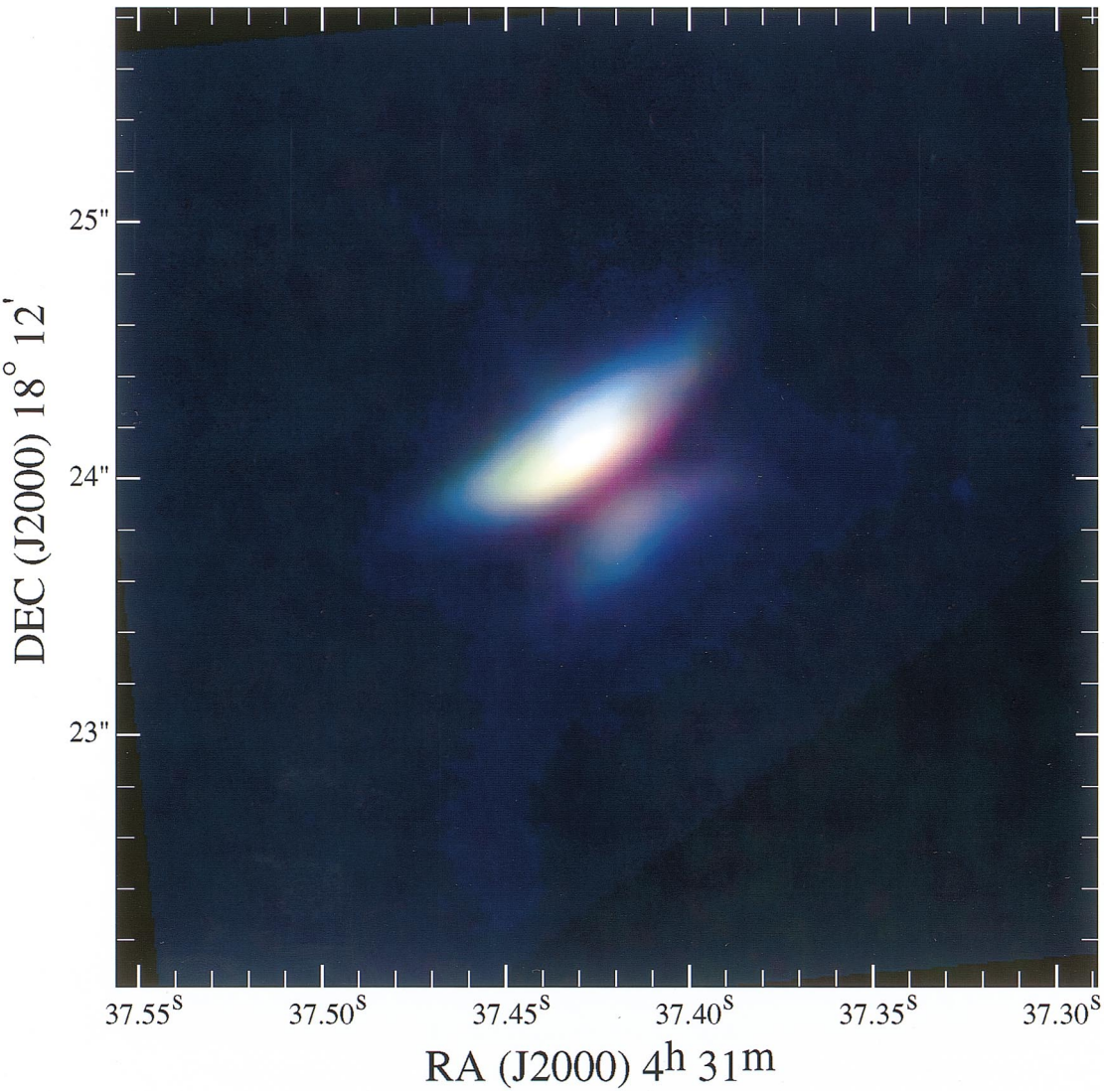

FIG. 2.—Three-color composite image of HH 30. WFPC2 F675W is blue, NICMOS F110W is green, and NICMOS F204M is red. This figure clearly illustrates how the lateral asymmetry of the nebula has changes with time. The WFPC2 image was taken in 1998 December; the NICMOS data were obtained in 1997 September.

as the zero point of the y-axis and the jet axis as the zero point of the x-axis. We use this coordinate system in Figures 5–10. The midplane of the disk, the zero point of the y-axis, has been set by determining the average position of the minima of emission in the F160W image (the determined average for F160W has the smallest uncertainties and is between the average minima of the F204M and F110W images). Since our data do not show the jet unequivocally, the origin of the x-axis was set using the position of the minimum disk thickness in the F110W image (the disk in the F110W image shows the largest variation in thickness providing the most accurate measurements of the minimum position). The derived position is very near that of the jet, which is seen best as a slight protrusion in the F110W image. Finally, the north-northeast lobe is taken as the upper lobe, and the south-southwest lobe is taken as the lower lobe. Subsequent discussion will use this coordinate system and nomenclature to discriminate between the features of interest.

3.1. *Photometry and Extinction*

Polygon photometry was obtained for the upper and lower lobes and is presented in Table 2, with the regions used for the photometry illustrated in Figure 5. To derive an upper limit on line-of-sight extinction toward HH 30, although not within the circumstellar disk, we assumed that since a typical stellar type in the Taurus-Auriga region is an M0 star with $T_{\rm eff} = 3850$ K (Wood et al. 1998), an M0 V model atmosphere would provide the best estimate of the actual stellar spectrum. As a class II young stellar object, however, HH 30 undoubtedly has infrared excess, and using an M0 V photosphere model spectrum to determine reference intrinsic colors will artificially increase the derived extinction at NIR wavelengths (Greene & Meyer 1995). Therefore, in using an M0 V spectral type as a reference star when estimating the intrinsic colors of HH 30, we will be deriving an upper limit on the extinction to the observed source. We derived the colors for an M0 V star at the distance of HH 30 by convolving the NICMOS filters with the appropriate 1993 Kurucz Stellar Atmosphere Atlas model (Table 2).[6] Using the color differences between our mea-

[6] The 1993 Kurucz Stellar Atmosphere Atlas is available from STScI at ftp://ftp.stsci.edu/cdbs/cdbs2/grid/k93models.

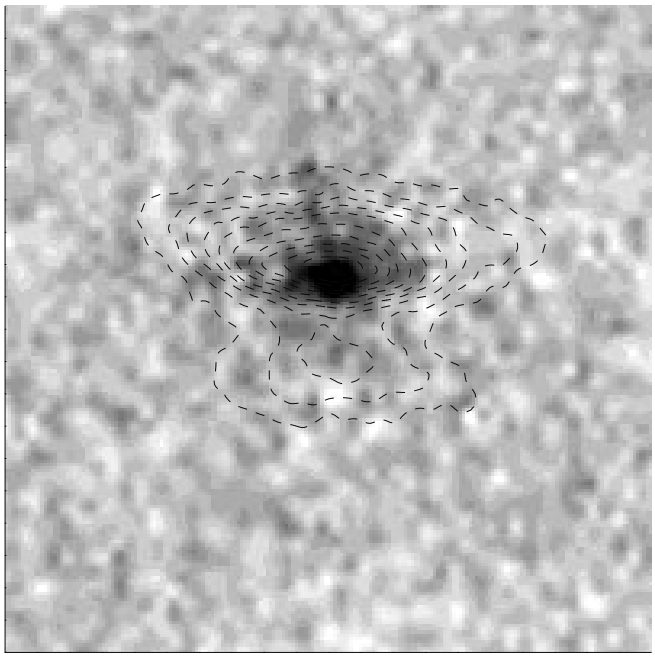

FIG. 3.—Inverted gray-scale image of the continuum-subtracted F212N H_2 image. The image has been overlaid with contours from the F204M image. The orientation of the image is that given in Fig. 5. The peak of the continuum image corresponds to H_2 emission, and a very faint trace of the jet can be discerned going up from the peak.

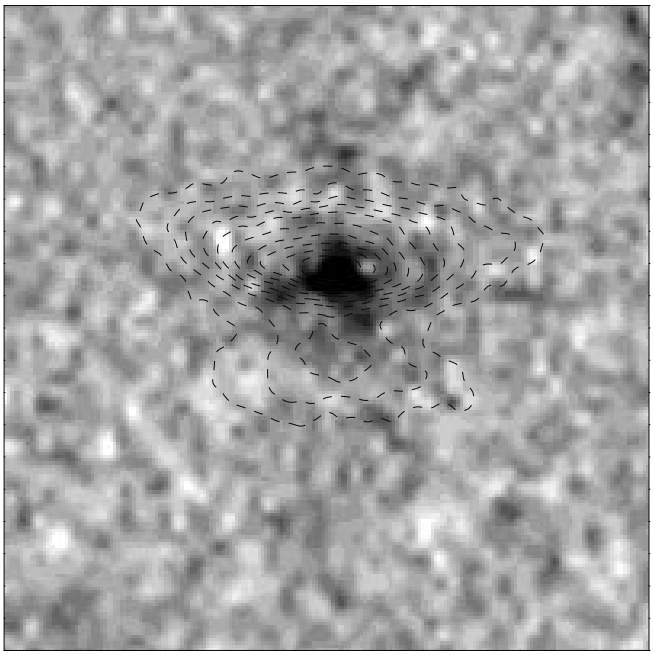

FIG. 4.—Inverted gray-scale image of the continuum-subtracted F187N Paα image. The image has been overlaid with contours from the F204M image. The orientation of the image is that given in Fig. 5.

surements and the selected reference M0 V star, in conjunction with the interstellar extinction law of Rieke & Lebofsky (1985), spline interpolated to the central wavelengths of the relative NICMOS filters (see Table 1), we derive an extinction of $A_V = 4.1 \pm 0.9$ along the line of sight to the region. This extinction is consistent with other stars in the Taurus-Auriga cloud, but we reiterate that this is an upper limit.

Even though we do not detect the star in the F204M filter, we can still use the observed flux at the presumed location of the star (the origin of the coordinates in Fig. 5) to estimate a lower limit on the extinction within the dust lane of HH 30. If we can determine the minimum magnitude of a star we *would* have been able to distinguish in our images, we can derive an observational lower limit on the extinction within the dust lane. There are two important caveats to this approach: (1) we have no way of knowing the exact unextincted magnitude of the star and therefore assume a K-band magnitude of ~ 9, typical for class II stars in the Taurus-Auriga Cloud (Kenyon & Hartmann 1995);

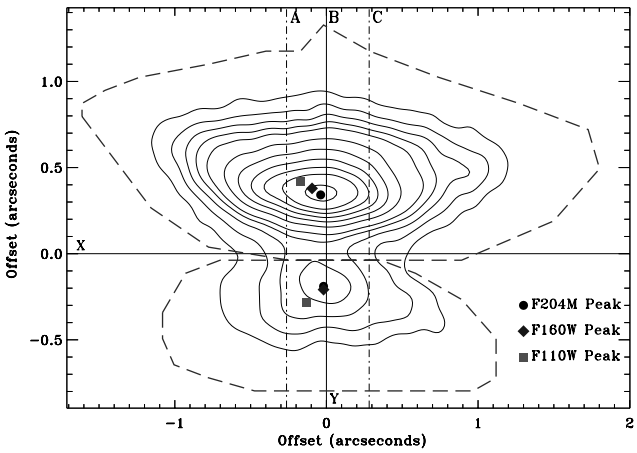

FIG. 5.—Schematic of HH 30 with the coordinate axis defined by the jet and midplane of the disk. The solid contours correspond to the F204M image; the dashed lines give the region used to determine the photometry in all images. [*See the electronic edition of the Journal for a color version of this figure.*]

TABLE 2

PHOTOMETRY

Source Name	F204M K[a]	F110W–F160W (J–H)[a]	F160W–F204M (H–K)[a]	F110W–F204M (J–K)[a]
M0V (at 140 pc)	8.26	0.91	0.24	1.15
Northeast lobe: observed	14.20	1.34	0.57	1.92
Southwest lobe: observed	15.65	1.49	0.57	2.06
Northeast lobe: best-fit model	14.18	1.37	0.68	2.05
Southwest lobe: best-fit model	15.57	1.43	0.72	2.15
Star + inner disk: best-fit model.....	8.6 ± 0.5	0.9 ± 0.15	0.5 ± 0.1	1.4 ± 0.2

[a] Approximate standard band equivalent (see Table 1 for NICMOS filter specifications).

(2) the light we do see is all scattered light, so the derived extinction values are a lower limit, representing a best estimate based on the available data.

Using the Tiny Tim code (Krist & Hook 1997), we created an artificial PSF with parameters that match our observations for all of the observed filters. These artificially created PSFs were also used when convolving our radiative transfer models (see § 4) for comparison with the data. Using IDP3, we added the artificial stellar PSF scaled to a known magnitude in the F204M filter. If we add a PSF star with a F204M magnitude of ~ 18.9, the star is detectable above the background; this is, therefore, the minimum stellar magnitude we could have detected at the longest wavelength. Using the assumed intrinsic magnitude and our interpolated interstellar extinction law, we derive a *lower limit* on the extinction of $A_{\rm F204M} \sim 9.9$, corresponding to $A_V \gtrsim 80$. This is considerably more than the lower limit of $A_V \sim 24$ derived by Burrows et al. (1996; and significantly higher than the $A_V = 30$ used in their models) but is consistent with the lower limit of $A_V \sim 80$ as suggested by Stapelfeldt & Moneti (1999). Yet another caveat is that the derived extinction assumed an ISM extinction law, which is unlikely to be correct given the results of our investigation of the dust opacity in the disk, as discussed below.

The best estimate of the actual extinction within the dust lane is that derived from our radiative transfer models of the scattered light (see § 4) based on the assumed density distribution of the dust in the disk, our viewing angle through the disk, and the opacity law of the dust. The extinction is computed by comparing the amount of direct (unscattered) light escaping the system at our viewing inclination to the stellar flux emitted into this direction, that is, $A_V = -2.5 \log (F_d/F_*)$. This is more accurate than integrating the optical depth through the envelope since it accounts for the emitting area of the star that sees different paths through the disk. Using this method, through our best-fit model, we calculate an extinction of $A_V \sim 7900$.

3.2. *Lateral Asymmetry*

As stated earlier, Stapelfeldt et al. (1999) reported a lateral asymmetry in the upper nebula in their 1998 WFPC2 image of HH 30. We also find a lateral asymmetry in the NICMOS images, but *on the opposite side* to that reported by Stapelfeldt et al. (1999). The location of the peaks in the reflected emission for upper and lower lobes are plotted in Figures 5 and 6. As can be seen, the peaks move away from the origin with decreasing wavelength. The peak in the F204M filter image is actually very close to the zero point of the x-axis for both the upper and lower lobes. In the F110W image, the peak in the upper lobe is offset by $\sim 0\farcs2$ (28 AU) and $\sim 0\farcs14$ (20 AU) in the lower lobe, *both* in the negative x-direction. The increasing peak offset with decreasing

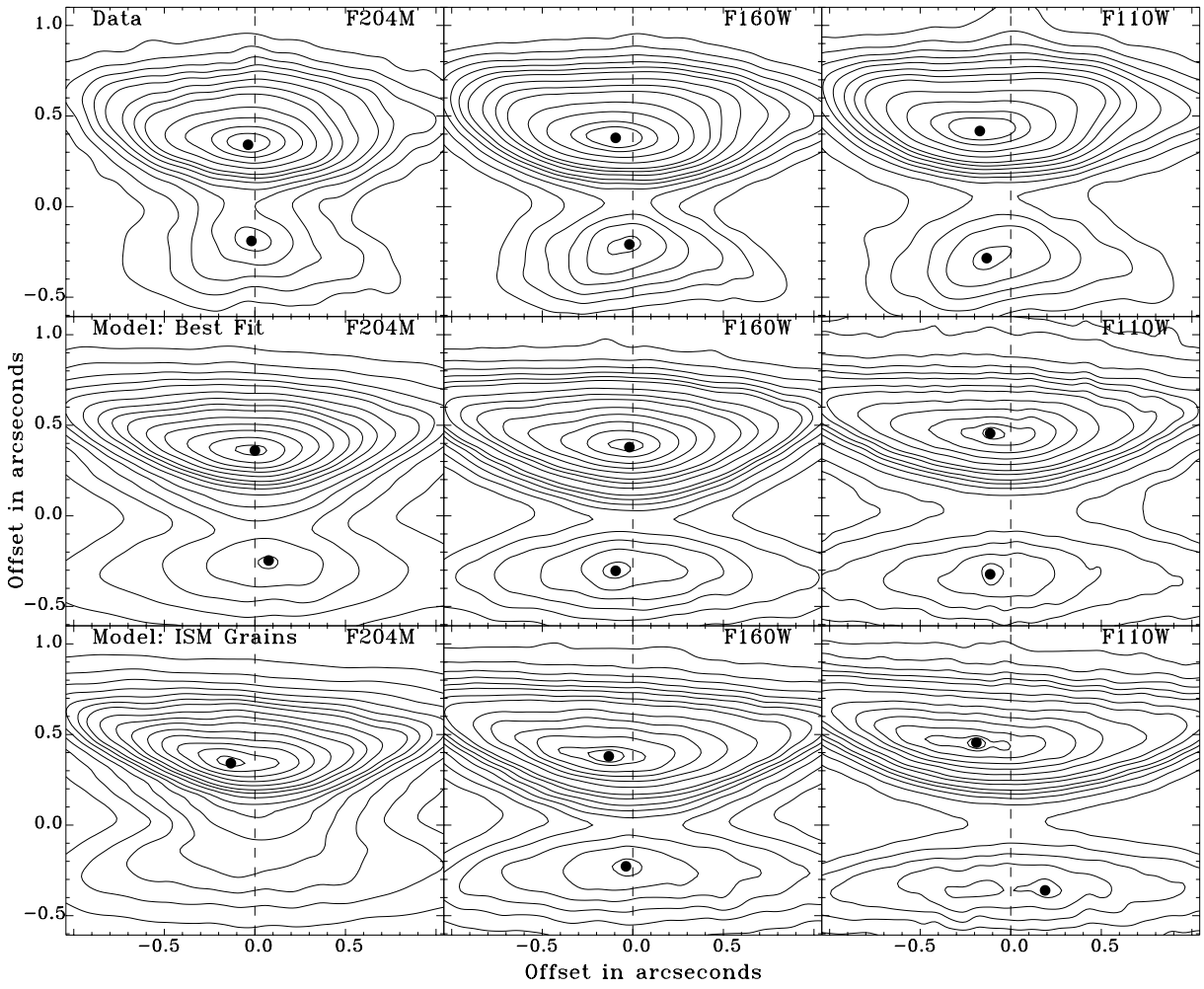

FIG. 6.—Contour maps of the data and models. Two different dust grain opacity parameters are shown: the best fit and the ISM grains. The filled circles indicate the derived peak positions. Contours have been scaled to illustrate clearly the positions of the peaks.

wavelength in the y-direction is easily explained by extinction due to dust in the disk. Since the asymmetry in the x-direction is undoubtedly related to the scattering by the disk, the supposition that the offset is caused by a simple difference in extinction from the disk is not satisfactory. One possible explanation is a wavelength-dependent variation in the forward-throwing scattering off the grains. Asymmetry in the x-direction has been noted previously (Burrows et al. 1996), and time-variable asymmetry has been both predicted and observed (Wood & Whitney 1998; Stapelfeldt et al. 1999). No indication of a wavelength dependence to this asymmetry, however, has been previously noted.

The peak of the scattered light in the WFPC2 F675W images moves from a negative x-axis position in 1994 to a positive x-axis position in 1998 (Stapelfeldt et al. 1999). The NICMOS observations were taken in late 1997 September. The timescale of the variations in the asymmetry has not been established, although the recent *VRI* monitoring of Wood et al. (2000) shows large variability on timescales of a few days. High-resolution synoptic imaging is required to test whether this unresolved photometric variability is related to the variability in the image morphology.

3.3. *Disk Morphology*

The location of the minimum emission in the disk, the maximum emission in the two nebular reflection lobes, and the total distance between the maxima have been determined for the data and the models and are presented in Figure 7. In Figure 7, the F204M data graph shows a jump in the location of reflection nebulosity maxima at $-0\farcs2$ for the lower lobe. There are, in fact, two peaks in the F204M emission in this region. This is illustrated more fully in Figure 8, where the two peaks in the line cut at position A are clearly illustrated (see Fig. 5 for line cut positions). This double peak is seen only in the F204M data. Figure 7 also illustrates that the rate of change of the disk thickness with distance from the assumed origin is asymmetric about *both* axes in the data. We note that the derived disk thickness varies by wavelength as expected, with a minimum difference between the maxima of the upper and lower lobes of $\sim$92 AU for F110W, $\sim$81 AU for F160W, and $\sim$74 AU for F204M.

Scattered-light models predict that the width of the dust lane should decrease with increasing wavelength (Wood et al. 1998), and thus multiwavelength imaging can be used to probe the disk mass and opacity. In Figure 8, the decrease in the width of the dust lane toward longer wavelengths is evident, and the lateral asymmetry is clearly seen: the cut at position A has a significantly higher intensity than the cut at position C. These vertical cuts also show that the upper and lower nebula are separated at all NICMOS wavelengths. This observation conflicts with the prediction in Wood et al. (1998) that the F204M band image should appear pointlike; i.e., a vertical intensity cut should show only a single peak and no dust lane. The scattered-light model of Wood et al. (1998) assumed a wavelength-dependent dust opacity that followed that of ISM grains—

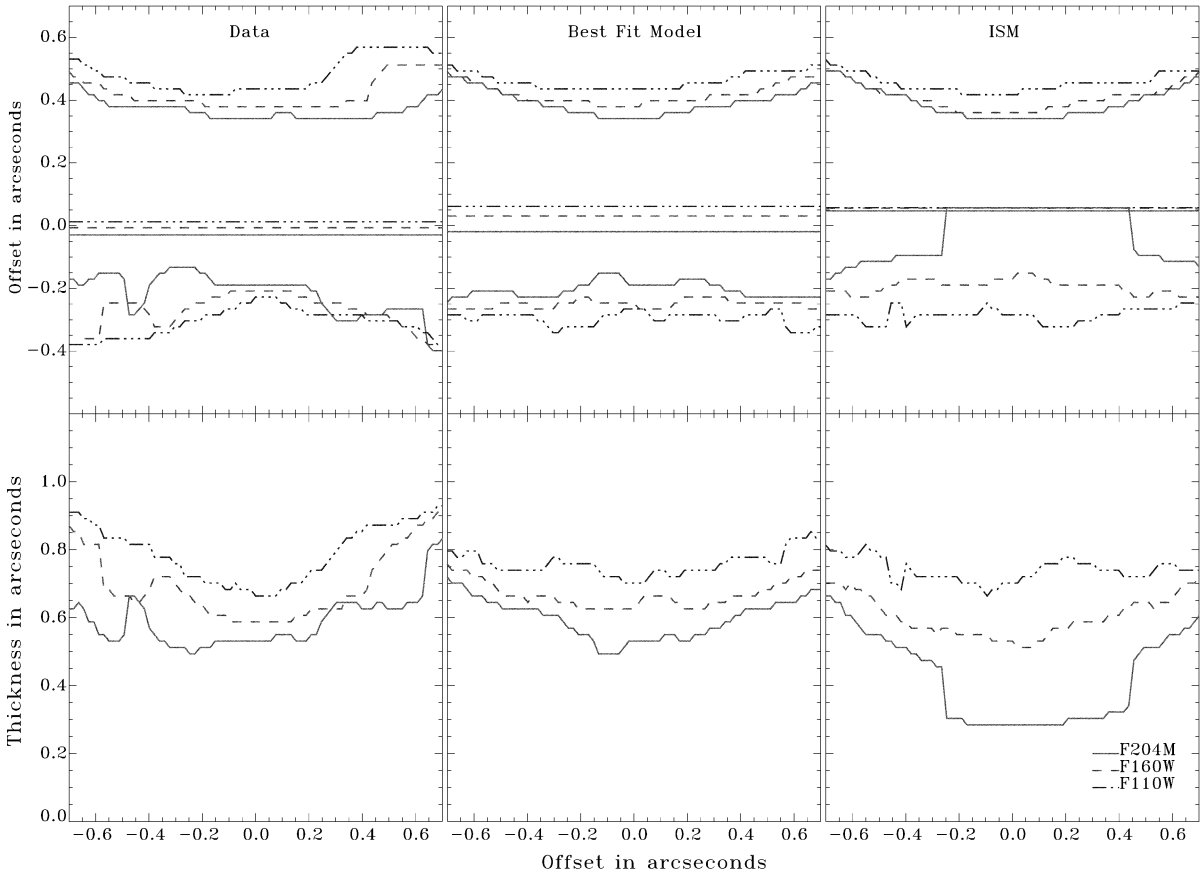

FIG. 7.—*Upper panel*: Location of the determined maxima for the upper and lower nebulae and the minima in the disk for the data and models as a function positional offset from the nominal center. *Lower panel*: Total disk thickness by filter taken as the total difference between the maxima of the upper and lower nebulae for the data and models as a function of offset along the x-axis. [*See the electronic edition of the Journal for a color version of this figure.*]

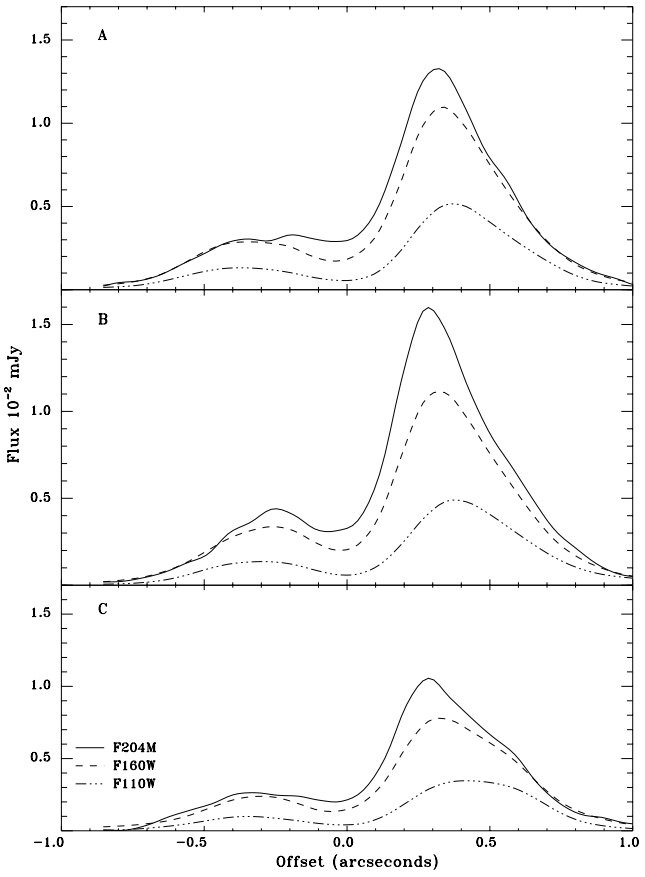

FIG. 8.—Line cuts at fixed x-axis locations across the upper and lower nebulae. The illustrated line cuts are at the positions indicated in Fig. 5. At position A, the double peak in the F204M filter image is clearly seen.

the new multiwavelength NICMOS images show that circumstellar dust in HH 30 must have a shallower opacity than ISM dust. A shallow wavelength-dependent opacity implies that larger grains sizes are needed (see, e.g., Hansen & Travis 1974). In § 4 we present new models for HH 30 that exploit this multiwavelength observational diagnostic to determine the circumstellar dust opacity.

3.4. H_2 *and* Pα *Emission*

The continuum-subtracted F212N image (Fig. 3) shows emission at the peak of the upper lobe of the reflection nebulosity and emission near the presumed location of the jet. At the peak, the total flux in a polygon of ~ 0.5 arcsec^2 is 0.13 ± 0.01 mJy. In the image there also appears to be two "blobs" along the axis of the jet, with the first somewhat elongated in the jet direction. The first blob has a flux level of $\gtrsim 5\ \sigma$, with σ being the statistical uncertainty based on the sky value, which is equal to the uncertainty quoted for the region above. The other more spherically symmetric blob a little farther north has a $\gtrsim 3\ \sigma$ flux level. The quoted values represent the largest derived uncertainty values and are consequently conservative. We therefore believe the H_2 emission we are seeing is real and may represent a detection of the jet within the region usually dominated by reflection nebulosity.

The continuum-subtracted F187N image (Fig. 4) also shows emission at the peak of the upper lobe but nothing at the location of the jet (which bolsters our confidence in the detection of the jet in H_2). In a polygon of ~ 0.4 arcsec^2 we derive a flux of 0.13 ± 0.02 mJy. In the WFPC2 Hα image, the jet is clearly seen (K. R. Stapelfeldt 2000, private communication), and the lack of jet emission at Paα is somewhat surprising.

4. MODELS

Previous modeling of optical images of the disk in HH 30 focused on determining the size, degree of flaring, and total mass of the scattering dust particles (Burrows et al. 1996; Wood et al. 1998). The asymmetries observed in the WFPC2 images and more recently the ground-based *VRI* variability have been modeled in the context of stellar hot spots that break the spherical symmetry of the disk illumination (Wood et al. 1998, 2000; Stapelfeldt et al. 1999). Also suggested as explanations for the asymmetry in the images are dust clouds near the source (Stapelfeldt et al. 1999) or nonaxisymmetric disk structure, but detailed models have yet to confirm these suggestions. The new NICMOS images enable us to further test the current disk and illumination models and provide multiwavelength coverage that allows an investigation of the wavelength dependence of the circumstellar dust opacity. The importance of this diagnostic, available only with high-resolution NIR data, is vividly illustrated by comparing the observed NICMOS F204M image with the prediction of Wood et al. (1998), whose model image at 2.2 μm is almost pointlike. Wood et al. assumed the dust opacity was one typical for ISM grains, which decreases by a factor of greater than 7 from the R band (6500 Å) to the K band (2.2 μm). The fact that the NICMOS images show a pattern characteristic of an optically thick disk demonstrates that the assumption of ISM dust grains is insufficient for HH 30—a flatter opacity law is required to fit simultaneously both the optical and NIR images.

In our modeling of the NICMOS images, we not only investigate different disk structures and illuminations but also alter the wavelength dependence of the dust opacity until we obtain a best fit to all the images. The scattered-light models have an image resolution of 10.57 AU pixel^{-1}, corresponding to the pixel scale of NICMOS at the distance of the nebula. We convolve each image with the relevant NICMOS Tiny Tim PSF to allow a direct comparison between the models and data.

4.1. *Disk and Stellar Structure*

The flared-disk geometry we adopt for our modeling is (Shakura & Sunyaev 1973)

$$\rho = \rho_0 \exp -\tfrac{1}{2}[z/h(\varpi)]^2/\varpi^{\alpha}\ , \qquad (1)$$

where ϖ is the radial coordinate in the disk midplane and the scale height increases with radius,

$$h = h_0(\varpi/R_*)^{\beta}\ . \qquad (2)$$

Recent detailed models of disk structure find that the scale height exponent varies with radius in the inner regions but follows a similar power law beyond a few AU (D'Alessio et al. 1999; Chiang & Goldreich 1997; Bell et al. 1997). The scattered-light models of Burrows et al. (1996) and Wood et al. (1998) demonstrated that high-resolution imaging enables the determination of the disk scale height at large radii. In particular, they noted that the scale height at a radius of 100 AU is $h_{100} \approx 15$ AU. Though the scale height h is constrained, the scattered-light models cannot discrimi-

nate between different combinations of h_0 and β that give the appropriate h.

We consider three different disk structures from the literature, each stipulating a different value for the flaring parameter β: $\beta = 9/8$ (Kenyon & Hartmann 1987), $\beta = 5/4$ (D'Alessio et al. 1999), and $\beta = 58/45$ (Chiang & Goldreich 1997). Our initial values of h_0 were chosen such that $h_{100} = 15$ AU and were then varied slightly to get the best-fitting image. The main differences between the resulting models were the amount of flux intercepted and scattered by the disk, with the highly flaring $\beta = 58/45$ disk scattering 2.7 times more than the $\beta = 9/8$ disk. We show the results for the $\beta = 58/45$ disk here, but note that all three flaring parameters give similar images as long as h_0 is changed so that h_{100} remains constant. We set $\alpha = 3(\beta - 0.5)$, which is the value appropriate for viscous accretion theory (Shakura & Sunyaev 1973). The circumstellar disk mass and opacity are variable parameters, with the required mass inversely proportional to the opacity. The resulting best-fit masses for the three flaring parameters were within 10% of each other.

In brief, the disk parameters were chosen based on theoretical models for hydrostatic structure in disks. The dust is assumed to be well mixed with the gas. The flaring exponent β is uncertain, but the combination of h_0 and β are well determined, giving $h = 15$ AU at a radius of 100 AU. The density exponent α is chosen based on theoretical models, and the combination of α and β does not significantly change the resulting mass required to fit the images. Our conclusion is that the disk structures assumed here are reasonable approximations to the structure observed in the HH 30 disk at radii greater than several AU. In the inner region, it is possible that nonaxisymmetric disk structures, dust clouds, and stellar hot spots could be contributing to the nonaxisymmetric nature of the illumination. We consider only hot spots in this paper.

Figure 9 presents a composite three-color image of our best model for the NICMOS images. This model adopts the single hot spot illumination as described in Wood et al. (2000), with spot temperature $T_s = 10^4$ K, stellar temperature $T_* = 3000$ K, spot size $\theta_s = 20°$, and spot latitude $\phi_s = 60°$. For disk parameters in this model, we use a disk scale height exponent of $\beta = 58/45$, density exponent $\alpha = 2.36667$, stellar radius $R_* = 2.5\ R_\odot$, inner radius $R_{\rm in} = 6\ R_*$, and scale height at the stellar surface of $h_0 = 0.011$. The disk extends to 200 AU in radius.

4.2. *Dust Properties*

The models are run at wavelengths corresponding to the effective wavelength for the F110W, F160W, and F204M filters (see Table 1). To insure that calculating the models at

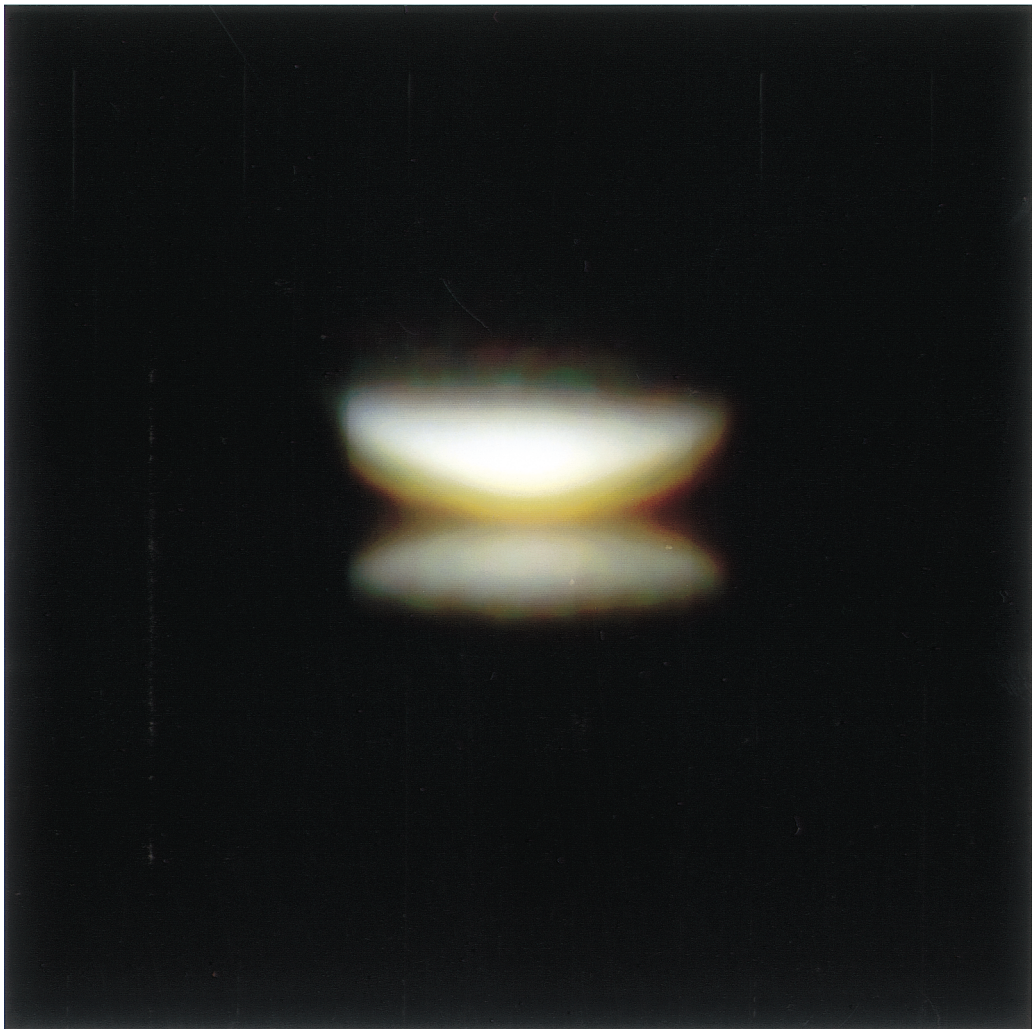

FIG. 9.—Three-color composite image of HH 30 models. The model F110W image is blue, F160W is green, and F204M is red.

a single wavelength is as accurate as calculating over the entire filter function, we ran a model finely spaced in wavelength and weighted the flux by the NICMOS filter functions. The result did not vary noticeably from simply using the filter effective wavelength.

The dust opacity was modified to fit the variations in the dust lane thickness as a function of wavelength. Altering the disk properties—scale height, flaring, and radial power law—has no effect on the wavelength-dependent width. The dust lane thickness is related to the optical depth of the dust, which is proportional to the opacity of the dust. As the opacity of the dust decreases at longer wavelengths, the dust lane width decreases. Our best model uses opacity ratios of $\kappa_{F110W}:\kappa_{F160W}:\kappa_{F204M} = 1.37:1.29:1.00$. This opacity law is flatter than that for ISM grains, which have $\kappa_{F110W}:\kappa_{F160W}:\kappa_{F204M} = 1.86:1.58:1.00$ (Kim, Martin, & Hendry 1994).

To obtain this opacity law, we computed a grain-size distribution consisting of homogeneous spheres composed of either amorphous carbon (Rouleau & Martin 1991) or revised astronomical silicate (Weingartner & Draine 2000). The size distribution for each component is specified using a power law with exponential decay [$r^{-p} \exp(-r/r_c)$; see, e.g., Kim et al. 1994] with a geometric cross section (πr^2) weighted average radius (summed over both components) of $r_{eff} = 0.056$ μm. The relative numbers of each grain type are such that the ratio of C to Si is roughly solar with a gas-to-dust mass ratio of 100. The absolute value of the opacities, and therefore the disk mass determination, depends on the assumed value of the gas-to-dust ratio, which is not well constrained in the circumstellar environment modeled here. The absolute value of the opacities are also sensitive to the exact nature of the size distribution. Since we are only modeling NIR wavelengths, we are effectively limiting our analysis to grains of the order of 1 μm in radius. Thus, our mass estimate is a lower limit; that is, we can imagine a population of much larger particles that dominate the disk mass but contribute little to the opacity at NIR wavelengths. What is certain in the models of the HH 30 disk is that the opacity law is flatter than that for interstellar grains, and this implies that the grains seen by NIR radiation are larger than those in the interstellar medium. The effective grain size in this population is about 2.15 times larger than standard ISM grains (Kim et al. 1994). This is consistent with the work of Burrows et al. (1996) and Wood et al. (2000), who found that the phase function for the dust is more forward-throwing.

The scattering phase function is calculated using the Mie theory for spherical particles. Tables of the scattering phase function are read into the Monte Carlo program and used to compute scattering directions in the radiative transfer. This is more precise than using the Henyey-Greenstein function for scattering but does not change the results significantly. Table 3 tabulates the grain properties. The opacity κ is given in units of cm^2 gm^{-1}. The albedo a is the ratio of scattering cross section to absorption cross section and thus a measure of how much light is scattered at each interaction. The average cosine of the scattering angle g quantifies the "forward-throwing" scatter from the dust; $g = 0$ is isotropic, and $g = 1$ is 100% forward-scattering. The maximum polarization obtainable for a given scatter, P, occurs at about a 90° scattering angle.

Figure 6 presents contour maps and the derived emission peaks for the data, the modified dust opacity model (best-fit), and the models that use an ISM opacity law. The ISM model used here differs from Wood et al. (1998) in that the disk mass is set at the wavelength of the F110W filter, 1.14 μm, instead of the R-band filter, 6500 Å. The disk mass required to fit the F110W image with ISM dust is 1.1×10^{-3} $M_\odot$, roughly 4 times larger than that required to fit the R-band image (Wood et al. 1998). Using this mass and ISM grains in an R-band model gives an image with too wide a dust lane, providing additional verification of our primary conclusion—the ISM dust opacity law is too steep to fit simultaneously the multiwavelength imaging data of HH 30. Figures 6 and 7 illustrate that even when using this increased disk mass with an ISM grain model, the longer wavelength F204M model image does not match the data image since no dust lane is produced. Figure 7 also illustrates how changing the circumstellar dust opacity as a function of wavelength determines the accuracy with which the model reproduces the width of the dust lane at the various wavelengths.

TABLE 3

PARAMETERS FOR DUST GRAINS

Wave Band	λ_{eff} (μm)	κ (cm^{2}g^{-1})	ω	g	P
Best-Fit Grains					
F110W	1.14	120.1	0.48	0.52	0.38
F160W	1.61	87.9	0.48	0.49	0.40
F204M	2.08	68.0	0.46	0.46	0.42
ISM Grains[a]					
KMH110.....	1.14	73.0	0.47	0.33	0.59
KMH160.....	1.61	39.2	0.41	0.28	0.59
KMH204.....	2.08	24.7	0.37	0.25	0.60

[a] Kim et al. 1994.

The shallow opacity law required to match the image morphology indicates the presence of larger-than-ISM grains, which is consistent with the evidence for grain growth in circumstellar environments found by other research groups (e.g., Burrows et al. 1996; Lucas & Roche 1998). Dust is expected to settle to the disk midplane, leaving only the smallest grains in the upper disk layers where most of the observed radiation scatters (see Ruden 1999 and references therein). Our result that a flatter opacity law is required suggests that coagulation has occurred since even the smallest grains in the upper layers are larger than standard ISM.

The circumstellar dust mass for our model is $M_{dust} = 6.7 \times 10^{-4}$ $M_\odot$, which is intermediate between the Burrows et al. (1996) and Wood et al. (1998) estimate. Again, we emphasize that we are estimating the mass of only those particles that efficiently scatter light at these wavelengths (the small grains) since larger particles are effectively invisible. Additional observations at millimeter and submillimeter wavelengths are needed to probe the mass of larger particles in the disk. In addition, our mass estimate depends on several uncertain parameters, such as the composition of the grains and the gas-to-dust mass ratio.

4.3. *Lateral Asymmetry*

The inclusion in the models of a hot spot reproduces the gross characteristics of the lateral asymmetry of the upper lobe (Fig. 6). The wavelength-dependent shifts in the emission peaks are generally reproduced with the modified dust

opacity models and noticeably less so in the ISM grain models. In the ISM grain model, for the lower emission lobe, no peak is produced for F204M, while two are produced for F110W, with the stronger peak on the opposite side from the data peak.

To investigate the more subtle differences between the models and data, Figure 10 shows the residual images formed by subtracting the models from the data. These images were produced by minimizing the statistical variance in the subtracted images using the same method as that used for continuum subtraction of the narrowband images: first the models were scaled to the data, then the alignment between the two images was adjusted until a minimum was obtained. The flux in these residual images represents $\lesssim 3\%$ of the *total* flux in the F110W and F160W NICMOS images and $\sim 10\%$ in F204M, demonstrating how well the models fit the data. In the localized regions where the discrepancies are more apparent, the residuals are generally $\sim 2\%$–4% larger.

A careful examination of Figure 10 produces a few noteworthy differences between the data and models. In both the F110W and F204M residual images, there is an enhancement along the central y-axis, arguably caused by emission from the jet that is not included in the models. The models are consistently wider and flatter in the lower nebula and stronger in the middle of the upper nebula than the data, which is most likely the result of asymmetries in the disk that were not included in the models. Overall, the models provide an excellent match to the observations, and these subtle variations are not surprising considering we have adopted an idealized, single hot spot and axisymmetric disk model.

4.4. *Properties of the Central Source*

If the central star is a normal T Tauri star, the scale factor used to fit the model flux to the data can also be used to derive an approximation of the intrinsic flux of the illuminating source. We assume the disk geometry and scattering properties of the dust are correct and estimate the intrinsic flux of the source in the different filters; the results are presented in Table 2. The error bars given for the F204M magnitude are due to the uncertainty in the flaring exponent of the disk; one magnitude spans the range of scattered flux given by reasonable flaring exponents (from 9/8 to 58/45). The error bars given for the colors are due to uncertainties in the reddening through the Taurus molecular cloud to the HH 30 disk (§ 3.1). The intrinsic colors derived for HH 30 are consistent with both normal T Tauri stars (Hartmann & Kenyon 1985) and T Tauri stars undergoing magnetic accretion (Kenyon et al. 1994). The intrinsic fluxes can be used to estimate the luminosity of the central star. Assuming a spectral type for the central source of M0 (Kenyon et al. 1994), a distance to the source of 140 pc, and colors and bolometric correction for an M0 source (Kenyon & Hartmann 1995), we calculate that the luminosity lies in the $L_{\rm bol} \sim 0.2$–$0.9\ L_{\odot}$ range. Our calculation was performed at the F110W wavelength (where emission from the disk is minimized) for a range of flaring parameters, $\beta = 9/8$–$58/45$, and assumed foreground extinction values, $A_V = 2$–4, hence, the range in luminosity.

5. SUMMARY AND DISCUSSION

We have presented *HST* NICMOS observations and detailed models of the scattered-light disk in HH 30. The

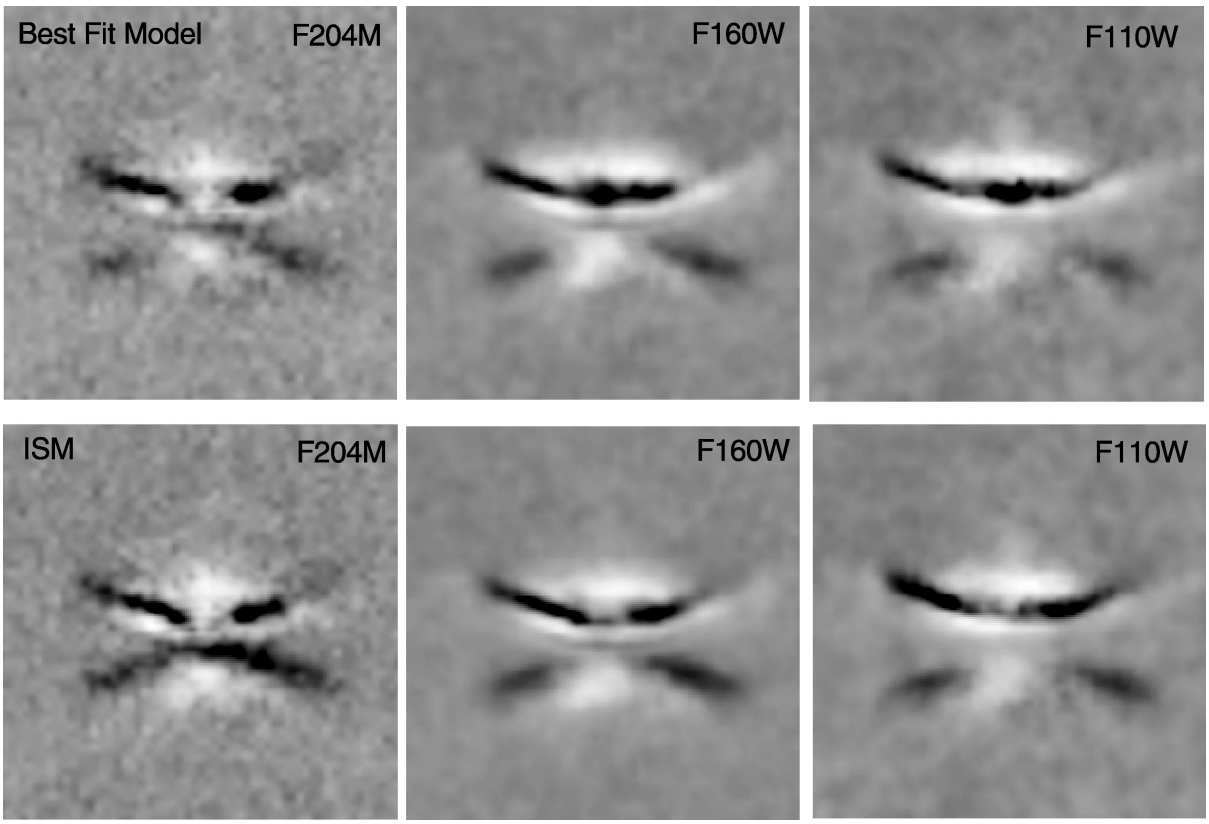

FIG. 10.—Residual images derived by subtracting the relevant models from the data. In both the F110W and F204M images, an enhancement along the central y-axis is likely emission from the jet, which is not included in the models. The total flux in the residual images is typically $\lesssim 5\%$ of the original flux.

NICMOS images show the characteristic scattered-light pattern of an optically thick, highly inclined circumstellar disk. There is a lateral asymmetry of the upper disk lobe that is on the opposite side to that seen in the 1998 WFPC2 images of Stapelfeldt et al. (1998). Modeling how the width of the dust lane changes with wavelength has enabled us to determine the NIR wavelength dependence of the circumstellar dust opacity. We find that the opacity variation with wavelength is more shallow than that of typical ISM grains. Thus, multiwavelength imaging provides a crucial diagnostic of circumstellar dust.

Our estimate for the mass of the circumstellar dust disk is $M_{\rm disk} = 6.7 \times 10^{-4}\,M_{\odot}$, but we caution that this represents a minimum mass since NIR observations are responsive only to small particles. The size distribution of large particles (i.e., rocks) is not constrained at these wavelengths (see § 4.2) and would contribute little to our derived opacity (D'Alessio, Calvet, & Hartmann 2001). A more massive disk would also result in a larger disk accretion rate (D'Alessio et al. 1999) and may be more consistent with the powerful jet observed in HH 30.

Comparison of the model fluxes to the data can be used to estimate the intrinsic T Tauri star flux and luminosity. The derived colors and fluxes (Table 2) are reasonable for a T Tauri star and suggest a luminosity of approximately 0.2–0.9 $L_{\odot}$. The model estimates $A_V \sim 7900$ through the disk, which is significantly larger than that derived from the photometry, which measures only scattered light from the disk, not direct stellar flux.

We have modeled the lateral asymmetry of the upper reflection nebular with a single hot spot on the stellar surface. This model is also consistent with the observed optical variability of 1.5 mag seen over a period of a few days (Wood et al. 2000). The asymmetry is variable, with the nebular shape appearing different in each epoch of the published WFPC2 data (Burrows et al. 1996; Stapelfeldt et al. 1999) and in our NICMOS images. The timescale of the morphological variability is as yet undetermined. High-resolution synoptic imagery is required to determine if the nebular variability is correlated with the photometric variability. The short timescale variability suggests changes occur very close to the star. One of the major goals in future monitoring of HH 30 should be to resolve whether this variability is caused by stellar hot spots, as presented above, or by shadowing of warps in the inner disk (Stapelfeldt et al. 1999).

We would like to thank NASA for both the telescope time and funding, without which none of the research for this paper would have been possible. A. S. C., E. Y., G. S., M. R., and R. T. acknowledge support under NAG 5-7923. We also acknowledge financial support from NASA's Long Term Space Astrophysics Research Program through grants NAG 5-6039 (K. W.) and NAG 5-8412 (B. A. W.), the National Science Foundation through grant AST 99-09966 (B. A. W. and K. W.), and the *HST* Archival Research Program through grant AR-08367.01-97A (B. A. W., K. W.). We thank Karl Stapelfeldt for providing the WFPC2 F675W image and for helpful comments. We also thank the anonymous referee for comments that improved the final manuscript.

REFERENCES

Adams, F. C., & Shu, F. H. 1986, ApJ, 308, 836
Beckwith, S. V. W., & Sargent, A. I. 1993, ApJ, 402, 280
Beckwith, S. V. W., Sargent, A. I., Chini, R. S., & Guesten, R. 1990, AJ, 99, 924
Bell, K. R., Cassen, M. P., Klahr, H. H., & Henning, Th. 1997, ApJ, 486, 372
Bertout, C. 1989, ARA&A, 27, 351
Bouvier, J., Cabrit, S., Fernandez, M., Martin, E. L., & Matthews, J. M. 1993, A&A, 272, 176
Burrows, C. J., et al. 1996, ApJ, 473, 437
Cameron, A. G. W. 1962, Icarus, 1, 13
———. 1973, Icarus, 18, 407
Cassen, P., & Moosman, A. 1981, Icarus, 48, 353
Chiang, E. I., & Goldreich, P. 1997, ApJ, 490, 368
Choi, P. I., & Herbst, W. 1996, AJ, 111, 283
D'Alessio, P., Calvet, N., & Hartmann, L. 2001, ApJ, 553, 321
D'Alessio, P., Calvet, N., Hartmann, L., Lizano, S., & Cantó, J. 1999, ApJ, 527, 893
Eaton, N. L., Herbst, W., & Hillenbrand, L. A. 1995, AJ, 110, 1735
Elias, J. H. 1978, ApJ, 224, 857
Ghosh, P., & Lamb, F. K. 1979a, ApJ, 232, 259
———. 1979b, ApJ, 234, 296
Greene, T. P., & Meyer, M. R. 1995, ApJ, 450, 233
Hansen, J. E., & Travis, L. D. 1974, Space Sci. Rev., 16, 527
Hartmann, L., & Kenyon, S. J. 1985, ApJ, 299, 462
Herbst, W., Herbst, D. K., Grossman, E. J., & Weinstein, D. 1994, AJ, 108, 1906
Kenyon, S. J., & Hartmann, L. 1987, ApJ, 323, 714
———. 1995, ApJS, 101, 117
Kenyon, S. J., et al. 1994, AJ, 107, 2153
Kim, S.-H., Martin, P. G., & Hendry, P. D. 1994, ApJ, 422, 164
Koerner, D. W., & Sargent, A. I. 1995, AJ, 109, 2138
Koerner, D. W., Sargent, A. I., & Beckwith, S. V. W. 1993, ApJ, 408, L93
Königl, A. 1991, ApJ, 370, L39
Krist, J. E., & Hook, R. N. 1997, The Tiny Tim User's Guide, Version 4.4 (Baltimore: STScI)
Krist, J. E., Stapelfeldt, K. R., Ménard, R., Padgett, D. L., & Burrows, C. J. 2000, ApJ, 538, 793
Lada, C. J. 1987, in IAU Symp. 115, Star Forming Regions, ed. M. Peimbert & J. Jugaku (Dordrecht: Reidel), 1
Lada, C. J., & Wilking, B. A. 1984, ApJ, 287, 610
Lucas, P. W., & Roche, P. F. 1998, MNRAS, 299, 699
Lynden-Bell, D., & Pringle, J. E. 1974, MNRAS, 168, 603
McLeod, B. 1997, in 1997 *HST* Calibration Workshop, ed. S. Casertano et al. (Baltimore: STScI), 281
Najita, J. 1995, in Rev. Mexicana Astron. Astrofis. Ser. Conf., 1, Circumstellar Disks, Outflows and Star Formation, ed. S. Lizano & J. M. Torrelles (Mexico, DF: Inst. Astron., UNAM), 293
Ostriker, E., & Shu, F. H. 1995, ApJ, 447, 813
Rieke, G., & Lebofsky, M. 1985, ApJ, 288, 618
Rouleau, F., & Martin, P. G. 1991, ApJ, 377, 526
Ruden, S. P. 1999, in The Origins of Stars and Planetary Systems, ed. C. J. Lada & N. D. Kylafis (Dordrecht: Kluwer), 643
Shakura, N. I., & Sunyaev, R. A. 1973, A&A, 24, 337
Shu, F., Najita, J., Ostriker, E., Wilkin, F., Ruden, S., & Lizano, S. 1994, ApJ, 429, 781
Stapelfeldt, K. R., Krist, J. E., Ménard, F., Bouvier, J., Padgett, D. L., & Burrows, C. J. 1998, ApJ, 502, L65
Stapelfeldt, K. R., & Moneti, A. 1999, in The Universe as Seen by *ISO*, ed. P. Cox & M. F. Kessler (ESA SP-427; Noordwijk: ESA), 521
Stapelfeldt, K. R., et al. 1999, ApJ, 516, L95
Stobie, E., Lytle, D., Barg, I., & Ferro A. 1999, in ESO Conf. Proc. 56, NICMOS and the VLT, ed. W. Freudling & R. Hook (Garching: ESO), 77
Terebey, S., Shu, F. H., & Cassen, P. 1984, ApJ, 286, 529
Weingartner, J. C., & Draine, B.T. 2001, ApJS, 134, 263
Wetherill, G. W. 1980, ARA&A, 18, 77
Whitney, B. A., & Hartmann, L. 1992, ApJ, 395, 529
Wichmann, R., Bouvier, J., Allain, S., & Krautter, J. 1998, A&A, 330, 521
Wood, K., Kenyon, S. J., Whitney, B., & Turnbull, M. 1998, ApJ, 497, 404
Wood, K., & Whitney, B. 1998, ApJ, 506, L43
Wood, K., Wolk, S., Stanek, K. Z., Leussis, L., Stassun, K., Wolff, M., & Whitney, B. 2000, ApJ, 542, L21